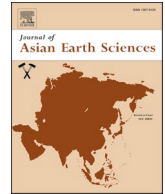




Contents lists available at ScienceDirect

Journal of Asian Earth Sciences

journal homepage: [www.elsevier.com/locate/jseas](http://www.elsevier.com/locate/jseas)

# Formation of the V-shaped conjugate strike-slip faults revealed by crustal anisotropy in the central Tibetan Plateau

Shitan Nie<sup>a,b</sup>, Jiangtao Li<sup>c,\*</sup>, Chenglong Wu<sup>a,b,\*</sup>, Ping Tan<sup>d,e</sup>

<sup>a</sup> State Key Laboratory of Lithospheric Evolution, Institute of Geology and Geophysics, Chinese Academy of Sciences, Beijing 100029, China

<sup>b</sup> Innovation Academy for Earth Science, Chinese Academy of Sciences, Beijing, China

<sup>c</sup> Department of Geophysics, School of Geodesy and Geomatics, Wuhan University, Wuhan 430079, China

<sup>d</sup> Institute of Disaster Prevention, Sanhe Hebei 065201, China

<sup>e</sup> Hebei Key Laboratory of Earthquake Dynamics, Sanhe Hebei 065201, China

## ARTICLE INFO

### Keywords:

The central Tibetan Plateau  
Seismic anisotropy  
Conjugate strike-slip faults  
Plastic deformation  
Crustal decoupling

## ABSTRACT

The dynamic processes responsible for the formation of the conjugate strike-slip faults in the central Tibet remain poorly understood. The crustal anisotropy can provide important constraints on the crustal deformation history and current state. Using data from a recently deployed seismic array (SANDWICH), we obtained crustal anisotropy results that reveal the deformation of the crust in the central Tibet with high resolution. The results show that most stations exhibit strong crustal anisotropy and nearly E-W fast orientations. Our results, when combined with previously revealed upper crustal anisotropy, indicates that the deformation in the upper and mid-lower crust is decoupled. The most prominent feature in our results is a weak crustal anisotropy belt along the BNS, suggesting the mid-lower crust has not undergone strong deformation. We propose that the combination of stable BNS and strong deformation on both sides of BNS in the mid-lower crust caused the formation of conjugate strike-slip faults.

## 1. Introduction

The Tibetan Plateau was created by the north–south convergence caused by the collision of the Indian and Eurasian plates since ~50 Ma (Yin and Harrison, 2000). Under the north–south compressional stress environment in the central Tibetan Plateau, the north–south trending rifts and conjugate strike-slip faults which indicate the east–west extension were developed (Tian et al., 2015; Yin and Taylor, 2011). These extensional structures play an important role in regulating the N-S shortening and E-W extension, especially the V-shaped conjugate strike-slip faults on both sides of the BNS (Taylor and Yin, 2009). Yin and Taylor (2011) proposed that the horizontal basal shear of the asthenospheric flow facilitate the formation of the conjugate strike-slip faults. However, the regionally dominant ENE-WSW oriented upper-mantle anisotropy beneath the conjugate strike-slip faults (Huang et al., 2000; Wu et al., 2019a) is not consistent with the E-W asthenosphere flow required by the basal shear model. High P velocity of upper mantle beneath the conjugate strike-slip faults also indicated that the horizontal basal shear from the asthenospheric flow could not act directly on the

crust, and speculated that the shear may come from the bottom of the upper crust rather than the lower crust (Nie et al., 2020). Then, does the eastward driving force come from the crustal flow? Some surface wave tomography results revealed relatively lower S velocities in the mid-lower crust beneath the conjugate strike-slip faults, which seemed to support the connection between crustal flow and the formation of conjugate strike-slip faults (Huang et al., 2020; Yang et al., 2012). However, magnetotelluric results show that the crust exhibited relatively high resistivity throughout the conjugate strike-slip faults, which may indicate that the degree of melting required by the crustal flow model does not exist beneath the BNS (Dong et al., 2020). More importantly, why do conjugate strike-slip faults occur on both sides of the BNS? Therefore, the formation mechanism of the conjugated strike-slip faults remains controversial.

One of the key constraints on the above questions is a high-resolution quantification of crustal deformation which can be obtained from the measurements of seismic anisotropy. Researchers have conducted a series of crustal anisotropy studies around the Tibetan Plateau (Chen et al., 2013; Hu et al., 2018; Kong et al., 2016; Shen et al., 2015; Sun et al.,

\* Corresponding authors at: State Key Laboratory of Lithospheric Evolution, Institute of Geology and Geophysics, Chinese Academy of Sciences, Beijing 100029, China (C. Wu).

E-mail addresses: [jiangtaoli@whu.edu.cn](mailto:jiangtaoli@whu.edu.cn) (J. Li), [wuchenglong@mail.iggcas.ac.cn](mailto:wuchenglong@mail.iggcas.ac.cn) (C. Wu).

<https://doi.org/10.1016/j.jseas.2023.105725>

Received 6 April 2023; Received in revised form 12 May 2023; Accepted 19 May 2023

Available online 20 May 2023

1367-9120/© 2023 Elsevier Ltd. All rights reserved.

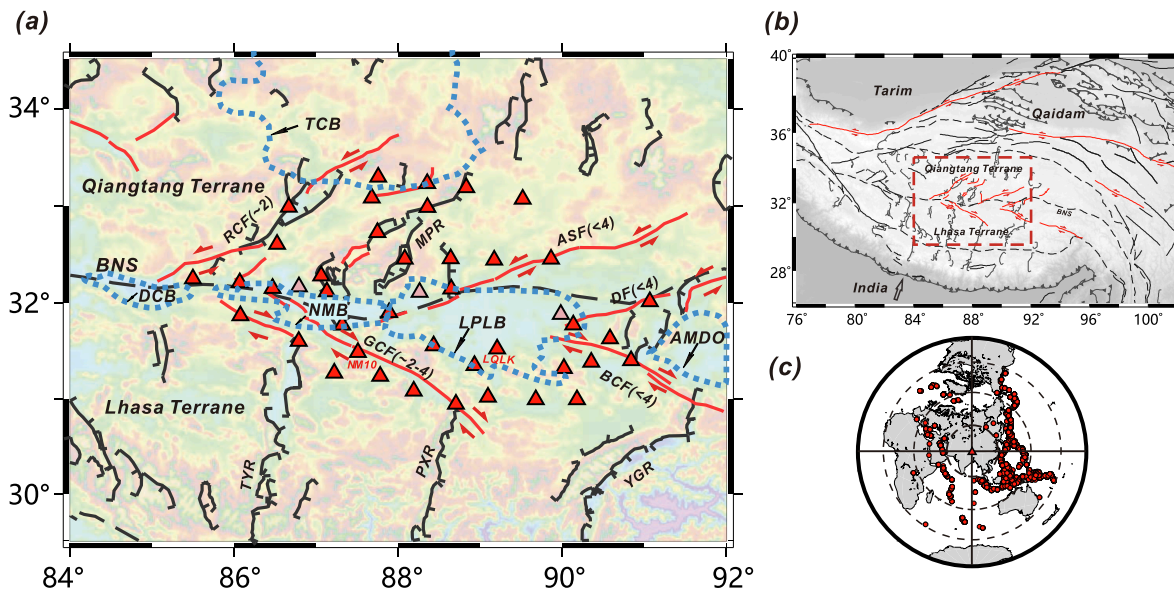


**Fig. 1.** Tectonic (Taylor and Yin, 2009) and topography map of Tibet with the SANDWICH seismic broadband stations used in this study. The blue dotted lines represent the locations of the basins. Red triangles display the SANDWICH seismic stations and the red words above the red triangles indicate the station name. Pink triangles represent stations failed to obtain the crust anisotropy due to insufficient azimuth coverage of receiver function. The slip rate of the faults (mm/years) are shown as the accompanying numbers (Wang et al., 2019). BNS = Bangong-Nujiang Suture, YGR = Yadong-Gulu Rift, PXR = Pumqu - Xianza Rift, TYR = Tangra Yum Co Rift. LPLB = Lunpola Basin, NMB = Nima Basin, AMDO = Amdo Block, TCB = Tuo Basin, DCB = Dongcuo Basin, MPR = Muga-Puruo Rift, GCF = Gyaring Co Fault, BCF = BangCo Fault, RCF = Ribug Caka Fault, ASF = Amdo-Selin Fault, DF = D Fault. Blue dashed lines represent the location of basin. (b) A map showing the location of the study area (the red dotted rectangle). (c) The location of the events used in this study (red circles). The red triangle shows the location of SANDWICH network. (For interpretation of the references to color in this figure legend, the reader is referred to the web version of this article.)

2015; Tan and Nie, 2021). However, due to the linearly distributed stations and limited acquisition time of seismic data, there are few crustal anisotropy studies in the conjugated strike-slip faults zone. The crustal anisotropy were only measured at some sporadic stations (Ozcar and Zandt, 2004; Sherrington et al., 2004; Wu et al., 2019a; Wu et al., 2015), which severely restricts the study on the formation of the conjugated strike-slip faults.

Pms splitting from receiver functions provides a measure of the average anisotropy and deformation within the whole crust since the Pms phase is generated at the Moho and the wave paths can be confined within the crust only (Kong et al., 2016). The fast direction and magnitude of the average crustal anisotropy can be obtained from the time variations of the P to S converted phases in the radial receiver functions.

Based on the broadband seismic stations data from the recent SANDWICH network (Liang et al., 2016), we obtain high-resolution crustal anisotropy in the central Tibetan Plateau. Combining the results of previous upper crustal anisotropy (Wu et al., 2019b), we can provide better understanding for the formation of the conjugate strike-slip faults and tectonic evolution of the Tibetan Plateau.

## 2. Data and methods

We use the data from the 2-D SANDWICH broadband seismic array, which consists of 53 stations (Liang et al., 2016) that began recording in November 2013 and finished in February 2017 (Fig. 1). The stations are distributed on both sides of the BNS from the northern Lhasa terrane to the southern Qiangtang terrane, and the spacing is approximately 40 km on average. We utilize the receiver functions derived from 5039 teleseismic seismic events with a minimum moment magnitude of 5.0. The epicentral distance of teleseismic events is in the range of 30°–90°. In order to eliminate the variation of the arrival times of Pms caused by different ray parameters, we perform the incident moveout corrections (Yuan et al., 1997) using the IASP91 model to compute the moveouts for Ps. All the radial receiver functions are corrected to a reference ray

parameter of 0.06 s/km. Subsequently, we stack the corrected radial receiver functions into back azimuthal bins of 5° to obtain uniform back-azimuthal (BAZs) coverage where there are clusters of receiver function traces (Kaviani and Rumpker, 2015). Besides, as suggested by Rumpker et al. (2014), the stations with back-azimuthal gaps larger than 90° in receiver functions should be excluded to ensure the recovery of  $\cos 2\theta$  feature. In this way, 14 out of 53 stations in total are removed.

The arrival times of the P-to-S converted phase vary systematically with the back-azimuth of the events when the crust is a single layer of anisotropy with a horizontal axis of symmetry (Liu and Niu, 2012; Rumpker et al., 2014):

$$t = t_0 + \Delta t = t_0 - \frac{\delta t}{2} \cos[2(\alpha - \varphi)]$$

where  $t_0$  represents the Pms central arrival time in the isotropic case,  $\Delta t$  is the offset caused by crustal anisotropy along the raypath beneath the station.  $\delta t$  is the delay time associated with the crustal anisotropy,  $\alpha$  is the back-azimuth of the receiver function, and  $\varphi$  is the fast polarization orientation. The splitting parameters associated with the crustal anisotropy are obtained through a grid-research of the combination of  $t_0$ ,  $\varphi$ , and  $\delta t$  that gives the maximum amplitude of the stacked radial receiver functions (Liu and Niu, 2012; Rumpker et al., 2014).

For a dipping Moho and anisotropy with a horizontal axis of symmetry, the back-azimuthal variation of the arrival times of Ps can be fitted by a combination of  $\cos\theta$  and  $\cos 2\theta$  functions (Li et al., 2019; Tan and Nie, 2021):

$$t = t_0 + \Delta t = t_0 + \frac{\delta t_1}{2} \cos(\alpha - \varphi_1) - \frac{\delta t_2}{2} \cos 2(\alpha - \varphi_2)$$

where  $t_0$  represents the central arrival time,  $\Delta t$  is the offset caused by crustal anisotropy along the ray path beneath the station and the dipping Moho.  $\delta t_1$  is related to the dip angle and  $\varphi_1$  is related to the dip direction.  $\delta t_2$  is related to the strength of anisotropy and  $\varphi_2$  is related to the strike of the fast axis.

In order to make sure the reliability of the crustal anisotropy results,

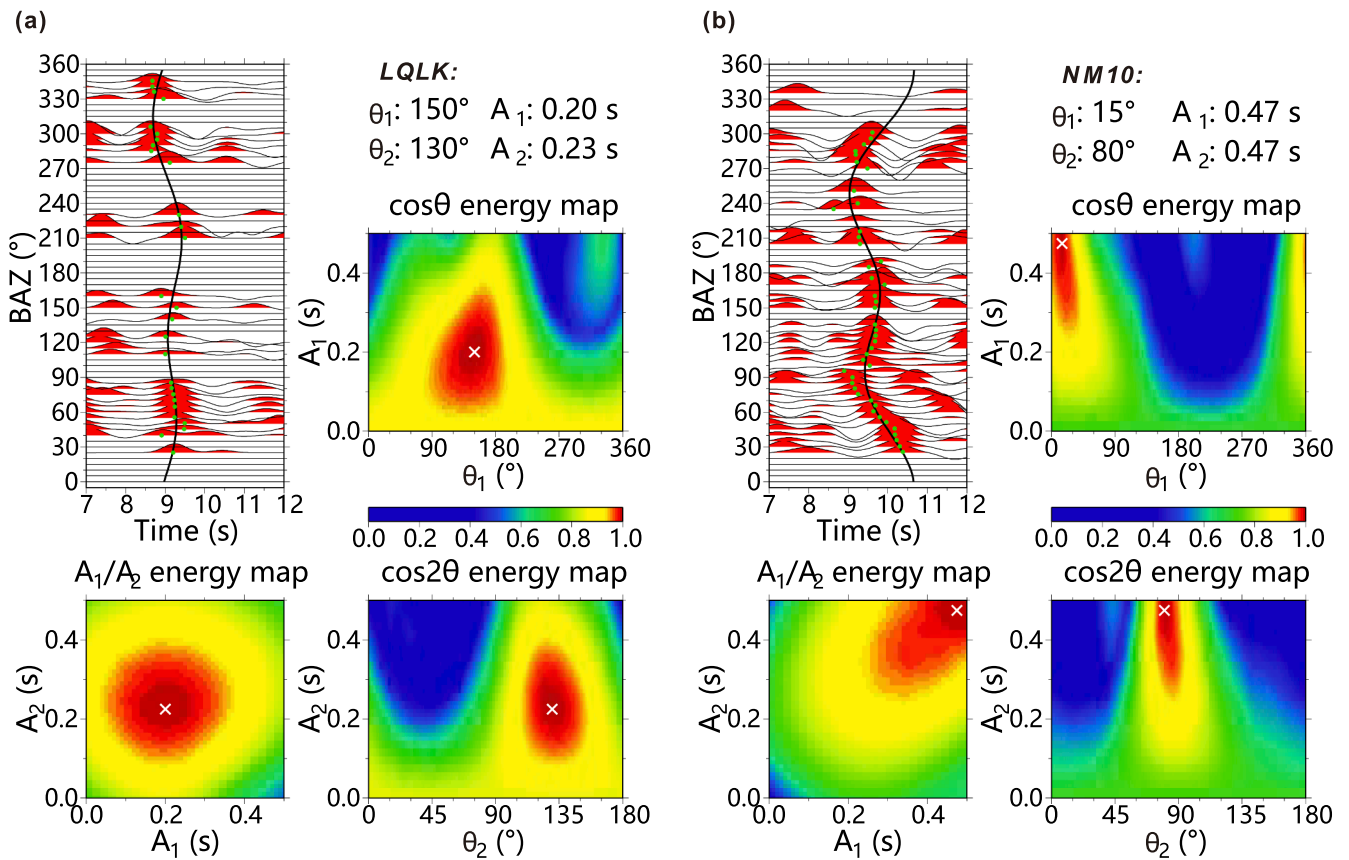


**Fig. 2.** Measurements of crustal anisotropy using Pms wave arrival times recorded by stations LQLK (a) and NM10 (b). The traces of the radial receiver functions against the back-azimuth (BAZ) are plotted on the left of each plot. The green dots represent peak values of Pms and the black curve represents the theoretical Pms moveout estimated by the cosine function using the optimal pair of splitting parameters. The color diagrams on the right and down of each plot show the stacking amplitudes calculated as a function of all candidate pairs of fast polarization directions and delay times. The cross points mark the locations of the peak amplitudes in each case, i.e. the optimal pair of parameters. The corresponding values of the splitting and dipping parameters are included on the top-right of each plot. (For interpretation of the references to color in this figure legend, the reader is referred to the web version of this article.)

synthetic tests with different crustal models (Table S1) are conducted. The parameters of the models are shown in Table S1, including isotropic and flat Moho (SYN1), dipping Moho (SYN2), anisotropic (SYN3), a combination of dipping Moho and anisotropic (SYN4). The synthetic three-component records are calculated based on the Raysum algorithm (Frederiksen and Bostock, 2000) with ray parameter of 0.06 s/km. Fig. S1 shows the radial receiver functions and the back azimuthal variation of the arrival times of Pms show obvious periodic variations. Based on the harmonic analysis of the Pms phase, the strength and direction of the crustal anisotropy can be well recovered.

Considering that the depth of Moho in the central Tibet is within 50–80 km (Kind et al., 2002; Liu et al., 2021; Lu et al., 2015; Nábelek et al., 2009; Shi et al., 2016; Tian et al., 2015), we searched  $t_0$  in the 5–12 s range with an increment of 0.1 s,  $\varphi_1$  in the 0–360° range and  $\varphi_2$  in the 0–180° range with 1° increments. The search range of  $\delta t_1$  and  $\delta t_2$  were set to 0–1.5 s with a step of 0.05 s. Some examples can be found in Fig. 2. The results of other stations are shown in Fig. S2.

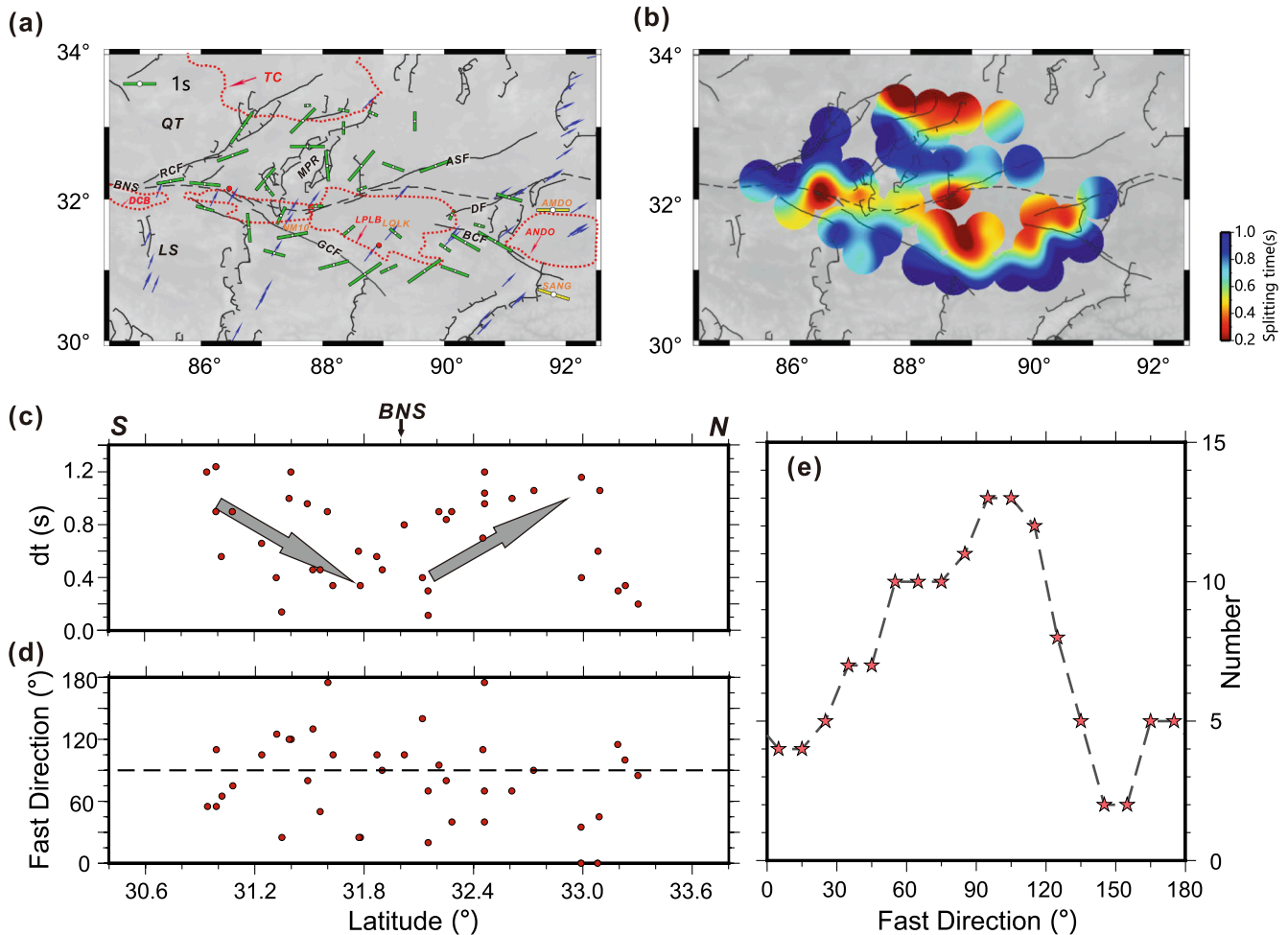
### 3. Results

Fig. 3a shows the corresponding Pms splitting measurements, containing both the fast-axis orientations and the time delay. The time delay in each station varies between 0.1 s and 1.4 s, with an average of  $0.654 \pm 0.288$  s. Our results show that the crustal anisotropy has block characteristics, which indicates that the deformation in different regions may be different (Fig. S3). The crustal anisotropy direction of Qiangtang terrane is mainly NE-SW, while that of Lhasa terrane is mainly NW-SE (Fig. S3). The most obvious feature in our results is a weakly crustal

anisotropic belt beneath the BNS, including the Lunpola Basin and Nima Basin, with an average anisotropy of 0.3 s (Fig. 3b). Weak crustal anisotropy also appears in the Tuco Basin within the Qiangtang terrane, with an average time delay of 0.28 s and fast orientations of dominantly E-W. However, the regions on both sides of the BNS (northern Lhasa terrane and southern Qiangtang terrane) show pronounced strong crustal anisotropy. In the northern Lhasa terrane, the  $\varphi_2$  measurements are dominantly NEE with a mean value of 0.84 s between 86° E and 90° E, which are nearly perpendicular to the trend of strike-slip faults. However, the anisotropic fast-axis orientations of the stations east of 90° E obviously changed to NWW, which are parallel to the trend of strike-slip faults with an average time delay of 0.72 s (Fig. S3) and consistent with the mid-lower crustal anisotropy from Sherrington et al. (2004) (Fig. 3a). The transform of the anisotropic fast-axis orientations may be caused by the barrier in the southern Lunpola Basin.

In the southern Qiangtang terrane, the fast orientations beneath the RCF and ASF are consistent with the trend of strike-slip faults, showing NE-SW, and the average value is 0.93 s. However, the crustal anisotropy beneath the MPR is relatively more complex and relatively stronger, which may be related to the compression of the BNS and Tuco basin that resulted in stronger crustal deformation.

To clearly analyze the variations of the anisotropy results, we also display the parameters of crustal anisotropy with respect to latitude of stations in Fig. 3c and d. The results also clearly show that the crustal anisotropy is weak beneath the BNS. We count the number of fast directions within each 30° window (Fig. 3e), which suggests that the anisotropic fast-axis direction is mainly eastward.



**Fig. 3.** (a) Crustal anisotropy (green bars of different length) at SANDWICH stations drawn on a topographic map. Red circles represent stations with crustal anisotropy of less than 0.2. The scale for delay times is shown in top-left legend. Blue arrows represent Global Positioning System (GPS) velocities from Gan et al. (2007). The yellow bars represent the middle-lower crustal anisotropy (only fast directions) at Stations AMDO and SANG (Sherrington et al., 2004). (b) Spatial distribution of the splitting time measurements. (c) and (d) The variations of the crustal anisotropic splitting times and fast wave directions in N-S orientation across BNS. The gray arrows represent the trend of time delay. (e) The numbers of different fast orientations of crustal anisotropy with  $30^\circ$  windows. Red stars represent the center of the windows. (For interpretation of the references to color in this figure legend, the reader is referred to the web version of this article.)

## 4. Discussion

### 4.1. Decoupled upper and mid-lower crust in the central Tibetan Plateau

Numerous investigations demonstrated that seismic anisotropy is a nearly ubiquitous property of the Earth's crust and mantle (Savage, 1999; Silver, 1996). It is generally believed that seismic anisotropy in the upper crust is mostly related to shape preferred orientation of fluid-saturated vertical cracks (Crampin, 1981), which are sub-parallel to the maximum horizontal compression direction. In the middle-lower crust, due to the closure of cracks, seismic anisotropy is mostly produced by the lattice preferred orientation (LPO) of anisotropic minerals in response to shear deformation or crustal/channel flow (Tatham et al., 2008). The anisotropy of the Pms splitting we observed is the combined effect of the upper and mid-lower crust. Since our results are distributed near the conjugate strike-slip faults and rifts, it is necessary to analyze the primary source of seismic anisotropy.

Our results show that the crustal anisotropy beneath most stations in the study area is strong (Fig. 3a) and the fast-axis direction is mainly E-W orientation (Fig. 3e). Wu et al. (2019b) used the same stations to analyze the anisotropy of the upper crust and showed that the average value of the upper crust anisotropy is 0.15 s. Fig. S4 shows the comparison between our crustal anisotropy results with the anisotropy of the upper

crust. The anisotropy of the upper crust is significantly smaller than that of the entire crust, which indicates that the anisotropy of our results mainly come from the mid-lower crust.

The strength of a quartz-rich continental crust increases with depth in the upper crust and then decreases in the mid-lower crust (Chen and Molnar, 1983). The mid-lower crust in the plateau is weaker than a standard mid-lower crust due to higher temperature (Hacker et al., 2000; Wang et al., 2016). The distribution of regional earthquakes in the central Tibetan Plateau suggests that most events concentrated in the depth range of 0–20 km (Zhu et al., 2017), indicating a significant brittle deformation in the upper crust. The surface wave dispersion and receiver function results revealed a low-velocity layer in the mid-lower crust in the central Tibetan Plateau (Huang et al., 2020; Yuan et al., 1997), which indicated that the mid-lower crust here is weak. A recent study on amphibole (Ko and Jung, 2015) suggested that shear deformation or crustal flow in the mid-lower crust can result in azimuthal anisotropy. Magnetotelluric results showed high resistivity beneath the study area, which suggested plastic deformation instead of crustal flow in the mid-crust (Dong et al., 2020). Numerical simulation results also showed that the formation of strike-slip faults does not require weak mid-lower crustal flow (Pang et al., 2018). The velocity structure from receiver function and surface wave joint inversion also indicated the melt volume percentage in central Tibet is too low (<7%) to decrease

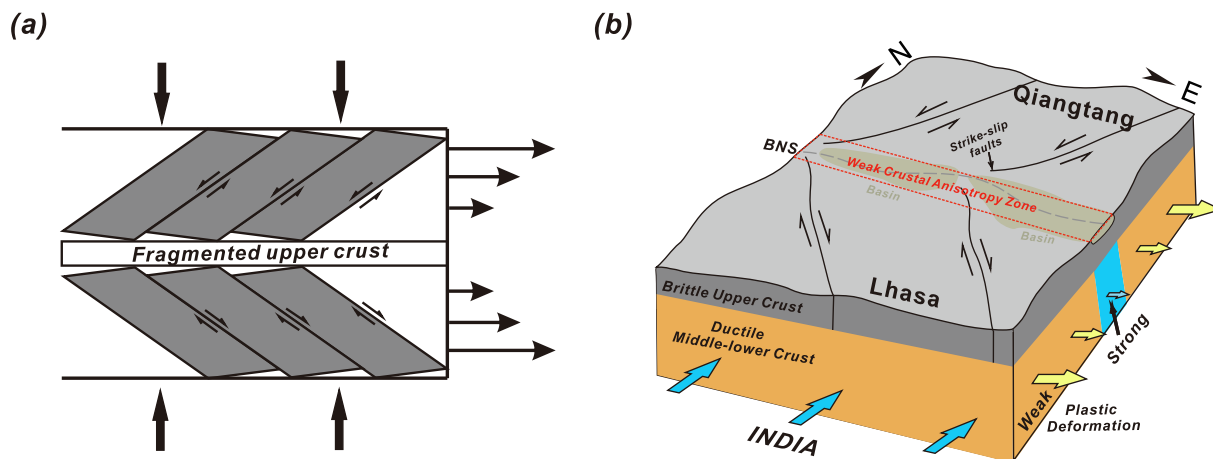


Fig. 4. Interpretation cartoon showing the extensional extrusion process in central Tibet. Fault rotation of upper crust via bookshelf-style faulting (a). (b) A three-dimensional (3-D) model showing the formation of V-shaped conjugate strike-slip faults.

rock strength enough to induce crustal flow (Nie et al., 2023). Combined with previous studies, we propose that (1) the seismic anisotropy observed in the study area is mainly contributed by the LPO of anisotropic minerals in the mid-lower crust, which is caused by shear deformation from the ongoing northward subduction of the Indian Plate, and (2) simple shear deformation may be the main mode of crustal deformation in the central Tibetan Plateau.

As the northward subduction of the Indian plate continues, the upper crust undergoes brittle deformation, while the mid-lower crust is weak and is prone to plastic shear deformation. The observed significant differences in the fast-axis directions of upper crustal anisotropy and average crustal anisotropy indicate that the upper and mid-lower crust in the central Tibetan Plateau are decoupled.

#### 4.2. The formation of the conjugate strike-slip faults

Yin and Taylor (2011) used a sandbox experiment to demonstrate the role of basal shear in generating V-shaped conjugate faults and proposed that the formation of the conjugate strike-slip faults come from the horizontal basal shear of the asthenospheric flow. However, the model simplifies the crust structure and considers the deformation of sand as the deformation of the crust. Therefore, the deformation difference between the weak mid-lower crust and the brittle upper crust on the Tibetan Plateau is ignored. The uppermost mantle velocity results showed high Pn velocity beneath the conjugate strike-slip fault zone, which also indicated that the horizontal basal shear from the asthenospheric flow could not act directly on the crust (Nie et al., 2020). In addition, the regionally dominant ENE-WSW oriented upper-mantle anisotropy (Huang et al., 2000; Wu et al., 2019a) is also different from the asthenosphere flow in the E-W direction required by the basal shear model (Yin and Taylor, 2011). Surface wave tomography and joint inversion of receiver function and surface wave results observed a low velocity layer in the mid-crust of the central Tibetan Plateau (Huang et al., 2020; Nie et al., 2023; Yang et al., 2012). The earthquake location results also showed that the earthquakes in the Tibetan Plateau are mostly distributed in the upper crust (within 20 km), and there are few earthquakes in the middle or lower crust (Langin et al., 2003; Zhu et al., 2017). These studies provided important evidence for a weak mid-lower crust in the central Tibetan Plateau. The strong crustal anisotropy and the mainly E-W fast-axis direction on both sides of the BNS (Fig. 3e) may be related to the N-S compression produced by the northward subduction of the Indian slab, which caused the east-west extension of the crust in the central Tibetan Plateau (Yin and Taylor, 2011). However, why the conjugate strike-slip faults only develop on the two sides of the BNS is still controversial. Our results show an obviously weak crustal

anisotropy belt beneath the BNS, which is consistent with the location of the basins (Lunpola and Nima Basin) on the BNS. The Lhasa and Qiangtang terrane reached an altitude of 4000 m at the beginning of the collision (Ding et al., 2014; Xu et al., 2013). However, Fang et al. (2020) used magnetostratigraphic and radiochronologic dating to revise the chronology of elevation estimates from the Lunpola Basin. They found the Lunpola and Nima Basin were still at a low elevation in the Eocene and probably stayed low until ~26 Ma ago, which suggests that the basins of the BNS uplifted late relative to the sides and thus relatively stable. Combined with the weakly anisotropic belt in our results, we believe that the mid-lower crust is stable and the crustal deformation is weak beneath the BNS.

In addition, the results of local body-wave tomography showed that the upper crustal velocity of the conjugate strike-slip faults is significantly lower than the rift areas in the south (Zhou et al., 2019). The distribution of earthquakes in the conjugate strike-slip faults area is diffuse and the magnitudes are small (Zhu et al., 2017), while the larger earthquakes are mainly developed to the south and north of the study area (Bai et al., 2017), which indicated that the upper crust of conjugate strike-slip faults area is weak and is not easy to accumulate stress and form large earthquakes. Weak upper crust under shearing of the mid-lower crust may be more prone to strike-slip fractures (Yin and Taylor, 2011). The results of Zhou et al. (2019) also showed that the lowest P velocities were along the basins in the BNS, which indicated that the upper crust of the BNS is fragmented. The fragmented upper crust of the BNS attenuated stress transmission between the upper crust of the Lhasa and Qiangtang terrane. Thus, V-shaped conjugate strike-slip faults can be developed on both sides of the BNS.

Combining the above information with surface geological structure, we propose a tectonic model that explains our crustal anisotropy results. The cartoon in Fig. 4 summarizes our interpretation of the relationship based on the previous discussion between the weak crustal anisotropy along the BNS and the formation of the conjugate strike-slip faults. Due to the northward subduction of the Indian slab, the weak mid-lower crust of the Lhasa terrane and Qiangtang terrane stretched in the nearly E-W direction, and then sheared the upper crust. Since the structure below the BNS is stable, the deformation of the crust beneath the BNS is weak. However, the crust far from the BNS region is strongly deformed and has a stronger tensile effect on the upper crust. Thus, the stable mid-lower crust beneath the BNS may be crucial for BNS as the center of the conjugate strike-slip faults. The strong crustal deformation on two sides of the BNS and stable crustal structure beneath the BNS may lead to the formation of conjugate strike-slip faults together.

## 5. Conclusions

According to the receiver function analysis, we obtained the crustal anisotropy in the central Tibetan Plateau. Based on the difference in the magnitude and direction of the previous upper crust anisotropy and our crustal anisotropy results, we suggested that the deformation of upper crust is mechanically decoupled from the mid-lower crust.

The crustal anisotropy results are characterized by a weak crustal anisotropy belt beneath the BNS (including the Lunpola and Nima Basin) which indicate the crust is stable. Strong crustal anisotropy on both sides of BNS may indicate the presence of plastic deformation. By a further combination with surface geological features and other seismological observations, we proposed that the combination of stable BNS and strong deformation on both sides of BNS resulted in the formation of the V-shaped conjugate strike-slip faults.

## Data availability statement

The receiver functions data used in this study are available at <http://zenodo.org/record/6860102#.YtZU2PnITog>.

## CRediT authorship contribution statement

**Shitan Nie:** Conceptualization, Methodology, Investigation, Writing – original draft, Validation, Funding acquisition. **Jiangtao Li:** Writing – original draft, Supervision, Investigation, Funding acquisition. **Chenglong Wu:** Visualization, Investigation, Supervision, Validation, Funding acquisition. **Ping Tan:** Writing – original draft, Investigation.

## Declaration of Competing Interest

The authors declare that they have no known competing financial interests or personal relationships that could have appeared to influence the work reported in this paper.

## Data availability

Data will be made available on request.

## Acknowledgements

This work was supported by the National Natural Science Foundation of China (Grant 42204063, 42174069, 41804058, 41904055). Most figures are plotted using the Generic Mapping Tools (Wessel and Smith, 1998).

## Appendix A. Supplementary material

Supplementary data to this article can be found online at <https://doi.org/10.1016/j.jseas.2023.105725>.

## References

- Bai, L., Li, G., Khan, N.G., Zhao, J., Ding, L., 2017. Focal depths and mechanisms of shallow earthquakes in the Himalayan-Tibetan region. *Gondwana Res.* 41, 390–399.
- Chen, W.-P., Molnar, P., 1983. Focal depths of intracontinental and intraplate earthquakes and their implications for the thermal and mechanical properties of the lithosphere. *J. Geophys. Res. Solid Earth* 88, 4183–4214.
- Chen, Y., Zhang, Z., Sun, C., Badal, J., 2013. Crustal anisotropy from Moho converted Ps wave splitting analysis and geodynamic implications beneath the eastern margin of Tibet and surrounding regions. *Gondwana Res.* 24, 946–957.
- Crampin, S., 1981. A review of wave motion in anisotropic and cracked elastic-media. *Wave Motion* 3, 343–391.
- Ding, L., Xu, Q., Yue, Y., Wang, H., Cai, F., Li, S., 2014. The andean-type Gangdese mountains: paleoelevation record from the paleocene-eocene linzhou basin. *Earth Planet. Sci. Lett.* 392, 250–264.
- Dong, H., Wei, W., Jin, S., Ye, G., Jones, A.G., Zhang, L., Jing, J.e., Xie, C., Yin, Y., 2020. Shaping the surface deformation of central and south Tibetan Plateau: Insights from Magnetotelluric array data. *J. Geophys. Res.: Solid Earth* 125, e2019JB019206.

- Fang, X., Dupont-Nivet, G., Wang, C., Song, C., Meng, Q., Zhang, W., Nie, J., Zhang, T., Mao, Z., Chen, Y., 2020. Revised chronology of central Tibet uplift (Lunpola Basin). *Science. Advances* 6, eaba7298.
- Frederiksen, A.W., Bostock, M.G., 2000. Modeling teleseismic waves in dipping anisotropic structure. *Geophys. J. Int.* 141, 401–412.
- Gan, W., Zhang, P., Shen, Z.-K., Niu, Z., Wang, M., Wan, Y., Zhou, D., Cheng, J., 2007. Present-day crustal motion within the Tibetan Plateau inferred from GPS measurements. *J. Geophys. Res.* 112, B08416.
- Hacker, B.R., Ghos, E., Ratschbacher, L., Grove, M., McWilliams, M., Sobolev, S.V., Wan, J., Zhenhan, W., 2000. Hot and dry deep crustal xenoliths from Tibet. *Science* 287, 2463–2466.
- Hu, J., Badal, J., Yang, H., Li, G., Peng, H., 2018. Comprehensive crustal structure and seismological evidence for lower crustal flow in the southeastern margin of Tibet revealed by receiver functions. *Gondwana Res.* 55, 42–59.
- Huang, S., Yao, H., Lu, Z., Tian, X., Zheng, Y., Wang, R., Luo, S., Feng, J., 2020. High-Resolution 3-D shear wave velocity model of the Tibetan Plateau: Implications for crustal deformation and Porphyry Cu deposit formation. *J. Geophys. Res.: Solid Earth* 125, e2019JB019215.
- Huang, W.-C., Ni, J.F., Tilmann, F., Nelson, D., Guo, J., Zhao, W., Mechie, J., Kind, R., Saul, J., Rapine, R., Hearn, T.M., 2000. seismic polarization anisotropy beneath the central Tibetan plateau. *J. Geophys. Res.* 105, 27979–27989.
- Kaviani, A., Rumpker, G., 2015. Generalization of the H- $\kappa$  stacking method to anisotropic media. *J. Geophys. Res. Solid Earth* 120, 5135–5153.
- Kind, R., Yuan, X., Saul, J., Nelson, D., Sobolev, S.V., Mechie, J., Zhao, W., Kosarev, G., Ni, J., Achauer, U., Jiang, M., 2002. seismic images of crust and upper mantle beneath Tibet evidence for Eurasian plate subduction. *Science* 298, 1219.
- Ko, B., Jung, H., 2015. Crystal preferred orientation of an amphibole experimentally deformed by simple shear. *Nat. Commun.* 6, 6586.
- Kong, F., Wu, J., Liu, K.H., Gao, S.S., 2016. Crustal anisotropy and ductile flow beneath the eastern Tibetan Plateau and adjacent areas. *Earth Planet. Sci. Lett.* 442, 72–79.
- Langin, W.R., Brown, L.D., Sandvol, E.A., 2003. Seismicity of central Tibet from project INDEPTH III seismic recordings. *Bull. Seismol. Soc. Am.* 93, 2146–2159.
- Li, J., Song, X., Wang, P., Zhu, L., 2019. A generalized H- $\kappa$  method with harmonic corrections on ps and its crustal multiples in receiver functions. *J. Geophys. Res. Solid Earth* 124, 3782–3801.
- Liang, X., Tian, X., Zhu, G., Wu, C., Duan, Y., Li, W., Zhou, B., Zhang, M., Yu, G., Nie, S., Wang, G., Wang, M., Wu, Z., Liu, Z., Guo, X., Zhou, X., Wei, Z., Xu, T., Zhang, X., Bai, Z., Chen, Y., Teng, J., 2016. SANDWICH: a 2D broadband seismic array in central Tibet. *Seismol. Res. Lett.* 87, 864–873.
- Liu, Z., Tian, X., Liang, X., Liang, C., Li, X., 2021. Magmatic underplating thickening of the crust of the southern Tibetan Plateau inferred from receiver function analysis. *Geophys. Res. Lett.* 48, e2021GL093754.
- Liu, H., Niu, F., 2012. Estimating crustal seismic anisotropy with a joint analysis of radial and transverse receiver function data. *Geophys. J. Int.* 188, 144–164.
- Lu, Z., Gao, R., Li, H., Li, W., Kuang, C., Xiong, X., 2015. Large explosive shot gathers along the SinoProbe deep seismic reflection profile and Moho depth beneath the Qiangtang terrane in central Tibet. *Episodes* 38, 169–178.
- Nábelek, J.G.H., Vergne, J., Sapkota, S., Kafle, B., Jiang, M., Su, H., Chen, J., Huang, B.-S., Team, T.H.-C., 2009. Underplating in the Himalaya-Tibet collision zone revealed by the Hi-CLIMB experiment. *Science* 325, 1371–1374.
- Nie, S., Tian, X., Liang, X., Chen, Y., Xu, T., 2020. Pn uppermost mantle tomography of Central Tibet: implication for mechanisms of N-S rifts and conjugate faults. *Tectonophysics* 788, 228499.
- Nie, S., Tian, X., Liang, X., Wan, B., 2023. Less-well-developed crustal channel-flow in the central Tibetan plateau revealed by receiver function and surface wave joint inversion. *J. Geophys. Res.: Solid Earth* 128.
- Ozacar, A.A., Zandt, G., 2004. Crustal seismic anisotropy in central Tibet: implications for deformational style and flow in the crust. *Geophys. Res. Lett.* 31, L23601.
- Pang, Y., Zhang, H., Gerya, T.V., Liao, J., Cheng, H., Shi, Y., 2018. The mechanism and dynamics of N-S rifting in southern Tibet: insight from 3-D thermomechanical modeling. *J. Geophys. Res. Solid Earth* 123, 859–877.
- Rumpker, G., Kaviani, A., Latifi, K., 2014. Ps-splitting analysis for multilayered anisotropic media by azimuthal stacking and layer stripping. *Geophys. J. Int.* 199, 146–163.
- Savage, M.K., 1999. Seismic anisotropy and mantle deformation: What have we learned from shear wave splitting? *Rev. Geophys.* 37, 65–106.
- Shen, X., Yuan, X., Ren, J., 2015. Anisotropic low-velocity lower crust beneath the northeastern margin of Tibetan Plateau: Evidence for crustal channel flow. *Geochem. Geophys. Geosyst.* 16, 4223–4236.
- Sherrington, H.F., Zandt, G., Frederiksen, A., 2004. Crustal fabric in the Tibetan Plateau based on waveform inversions for seismic anisotropy parameters. *J. Geophys. Res. Solid Earth* 109, B02312.
- Shi, D., Zhao, W., Klemperer, S.L., Wu, Z., Mechie, J., Shi, J., Xue, G., Su, H., 2016. West-east transition from underplating to steep subduction in the India-Tibet collision zone revealed by receiver-function profiles. *Earth Planet. Sci. Lett.* 452, 171–177.
- Silver, P.G., 1996. Seismic anisotropy beneath the continents probing the depths of geology. *Annu. Rev. Earth Planet. Sci.* 24, 385–432.
- Sun, Y., Liu, J., Zhou, K., Chen, B., Guo, R., 2015. Crustal structure and deformation under the Longmenshan and its surroundings revealed by receiver function data. *Phys. Earth Planet. In.* 244, 11–22.
- Tan, P., Nie, S., 2021. Crustal deformation in eastern margin of Tibetan Plateau from a dense linear seismic array. *Phys. Earth Planet. In.* 321, 106801.
- Tatham, D.J., Lloyd, G.E., Butler, R.W.H., Casey, M., 2008. Amphibole and lower crustal seismic properties. *Earth Planet. Sci. Lett.* 267, 118–128.

- Taylor, M.H., Yin, A., 2009. Active structures of the Himalayan-Tibetan orogen and their relationships to earthquake distribution, contemporary strain field, and Cenozoic volcanism. *Geosphere* 5, 199–214.
- Tian, X., Chen, Y., Tseng, T.-L., Klemperer, S.L., Thybo, H., Liu, Z., Xu, T., Liang, X., Bai, Z., Zhang, X., Si, S., Sun, C., Lan, H., Wang, E., Teng, J., 2015. Weakly coupled lithospheric extension in southern Tibet. *Earth Planet. Sci. Lett.* 430, 171–177.
- Wang, Q., Hawkesworth, C.J., Wyman, D., Chung, S.-L., Wu, F.-Y., Li, X.-H., Li, Z.-X., Gou, G.-N., Zhang, X.-Z., Tang, G.-J., Dan, W., Ma, L., Dong, Y.-H., 2016. Pliocene-Quaternary crustal melting in central and northern Tibet and insights into crustal flow. *Nat. Commun.* 7, 11888.
- Wang, H., Wright, T.J., Liu-Zeng, J., Peng, L., 2019. Strain rate distribution in South-Central Tibet from two decades of InSAR and GPS. *Geophys. Res. Lett.* 46, 5170–5179.
- Wessel, P., Smith, W.H.F., 1998. New, improved version of the generic mapping tools released. *Eos Trans. AGU* 79, 579.
- Wu, C., Tian, X., Xu, T., Liang, X., Chen, Y., Taylor, M., Badal, J., Bai, Z., Duan, Y., Yu, G., Teng, J., 2019a. Deformation of crust and upper mantle in central Tibet caused by the northward subduction and slab tearing of the Indian lithosphere: new evidence based on shear wave splitting measurements. *Earth Planet. Sci. Lett.* 514, 75–83.
- Wu, C., Tian, X., Xu, T., Liang, X., Chen, Y., Zhu, G., Badal, J., Bai, Z., Yu, G., Teng, J., 2019b. Upper-crustal anisotropy of the conjugate strike-slip fault zone in central Tibet analyzed using local earthquakes and shear-wave splitting. *Bull. Seismol. Soc. Am.* 109, 1968–1984.
- Wu, J., Zhang, Z., Kong, F., Yang, B.B., Yu, Y., Liu, K.H., Gao, S.S., 2015. Complex seismic anisotropy beneath western Tibet and its geodynamic implications. *Earth Planet. Sci. Lett.* 413, 167–175.
- Xu, Q., Ding, L., Zhang, L., Cai, F., Lai, Q., Yang, D., Liu-Zeng, J., 2013. Paleogene high elevations in the Qiangtang Terrane, central Tibetan Plateau. *Earth Planet. Sci. Lett.* 362, 31–42.
- Yang, Y., Ritzwoller, M.H., Zheng, Y., Shen, W., Levshin, A.L., Xie, Z., 2012. A synoptic view of the distribution and connectivity of the mid-crustal low velocity zone beneath Tibet. *J. Geophys. Res. Solid Earth* 117, B04303.
- Yin, A., Harrison, T.M., 2000. Geologic evolution of the Himalayan-Tibetan orogen. *Annu. Rev. Earth Planet. Sci.* 28, 211–280.
- Yin, A., Taylor, M.H., 2011. Mechanics of V-shaped conjugate strike-slip faults and the corresponding continuum mode of continental deformation. *Geol. Soc. Am. Bull.* 123, 1798–1821.
- Yuan, X., Ni, J., Kind, R., Mechie, J., Sandvol, E., 1997. Lithospheric and upper mantle structure of southern Tibet from a seismological passive source experiment. *J. Geophys. Res. Solid Earth* 102, 27491–27500.
- Zhou, B., Liang, X., Lin, G., Tian, X., Zhu, G., Mechie, J., Teng, J., 2019. Upper crustal weak zone in central Tibet: an implication from three-dimensional seismic velocity and attenuation tomography results. *J. Geophys. Res. Solid Earth* 124, 4654–4672.
- Zhu, G., Liang, X., Tian, X., Yang, H., Wu, C., Duan, Y., Li, W., Zhou, B., 2017. Analysis of the seismicity in central Tibet based on the SANDWICH network and its tectonic implications. *Tectonophysics* 702, 1–7.